Sticking Coefficient Effects on the Carbon Deposition Rates in an Electric Propulsion Testing Chamber

Gyuha Lim *, Huck Beng Chew † and Deborah A. Levin ‡
University of Illinois, Urbana-Champaign, Urbana, Illinois, 61801

Huy Tran§
Argonne National Laboratory, Lemont, Illinois, 60439

Ground testing is essential for understanding carbon sputtering caused by interactions between thruster beam ions and chamber walls. These interactions lead to back-sputtered carbon particles, which can contaminate the thruster. This study employs kinetic simulations with two distinct sputter models to analyze the deposition rate of back-sputtered carbon at the thruster exit. Previous studies have shown that yield models and angular distributions significantly influence sputtering behavior, often without considering the effects of sticking coefficients. In this work, we emphasize the role of energy distribution in determining deposition rates. Sticking coefficients, derived from molecular dynamics simulations as functions of incident energy and angle, are incorporated through post-processing the numerical results. While sticking coefficients from two different models are similar at normal incidence, our findings highlight a critical difference at high angles of incidence, we found that the Sigmund-Thompson energy distribution results in lower sticking coefficients compared to those derived from molecular dynamics based energy distributions. This discrepancy indicates that in future full chamber simulations using MD-based sticking coefficients, secondary carbon emissions from the sidewalls are likely to influence the deposition rate on the thruster.

I. Introduction

Electric propulsion (EP) technology holds immense promise for advancing human space exploration beyond low Earth orbit. However, its development faces significant hurdles, particularly in accurately replicating the space environment and assessing the operational lifetime of EP systems during ground testing. A key challenge lies in facility contamination, where carbon atoms back-sputtered from chamber walls are deposited onto thruster surfaces, distorting their lifespan. The high-energy plume emitted by thrusters interacts with these walls, leading to increased rates of back sputtering.

Nishii and Levin[1] recently addressed this challenge by modeling carbon sputtering based on a semi-empirical model by Yim[2, 3]. The simulations were performed using the Cuda-based Hybrid Approach for Octree Simulations (CHAOS): an octree-based Particle-In-Cell direct simulation Monte Carlo (PIC-DSMC) with MPI-CUDA parallelization[4]. Their results revealed that a symmetrical cosine angular distribution may overestimate carbon deposition rates to the thruster compared to the semi-empirical (SE) model.

Recently, Tran and Chew[5, 6] conducted molecular dynamics (MD) simulations to determine carbon sputtering yields under low-energy xenon ion bombardment. The previous study[8] integrated the MD sputter yield and its angular distribution in CHAOS successfully and investigated the back-sputtered carbon flux to the thruster exit region. While the SE model has a higher sputter yield, the deposition rate of the SE model was lower than the MD model since the angular distribution predicted by the MD model is more oriented to the thruster exit region than the SE model. While the angular distribution of the sputtered carbons affects the back-sputtered carbon flux significantly, the energy distribution of the sputtered carbons did not affect the back-sputtered fluxes when the sticking coefficient of carbons is assumed to be unity. This study applies the MD-based sticking coefficient in order to observe the effect of different energy distributions since the MD-based carbon sticking coefficient depends on the incident carbon energy and angle[6].

*Ph.D. Candidate, Department of Aerospace Engineering.
†Professor, Department of Aerospace Engineering.
‡Professor, Department of Aerospace Engineering.
§Postdoctoral Appointee, Applied Materials Division

II. PIC-DSMC Simulation in CHAOS

In a fully kinetic approach, Particle-In-Cell (PIC) simulation solves Poisson's equation to determine the electric field within the domain as

$$\nabla^2 \phi = -\frac{\rho}{\epsilon_0}, \tag{1}$$

$$E = -\nabla \phi. \tag{2}$$

The PIC simulation technique introduces super-particles representing groups of neutrals, ions, or electrons. The charge in each cell is calculated based on particles, and Poisson's equation is used to determine the potential and electric field in the domain.

While PIC simulations are suitable for collisionless plasmas, Serikov et al.[7] coupled the direct simulation Monte Carlo (DSMC) method with PIC to account for collisions using the No-Time-Counter (NTC) scheme to handle different time scales between PIC and DSMC simulations. This scheme addresses different time steps and weighting factors for ions and neutrals, as neutrals are only influenced by the collisions in the DSMC module, whereas ions are affected by both PIC and collisions. Thus, ions move every PIC iteration, and neutrals move when the DSMC module is called, every F_{col} number of the PIC iterations.

Weighting factors (W) also govern the time scale difference between ion and neutral species. This factor increases the number of ions and electrons compared to the neutrals to consider different length scales of plasma frequency for the PIC simulation and the mean collision time for the DSMC simulation to consider different time steps and weighting factors of the charged particles and neutrals. Thus, the relationship between the time steps of neutrals and ions becomes

$$\frac{W_n \cdot F_{col} \cdot \Delta t_i}{W_i \cdot \Delta t_n} = 1. \tag{3}$$

In this study, the DSMC module includes two types of momentum exchange (MEX) collisions: neutral-neutral and ion-neutral, and one type of charge exchange (CEX) collisions: ion-neutral. MEX collisions exchange momentum, while CEX collisions transfer charge, generating low-energy ions.

To overcome the computational costs of three-dimensional fully kinetic PIC-DSMC simulations, Jambunathan and Levin[4] introduced a linearized forest of octrees (FOT) with adaptive mesh refinement (AMR) in CHAOS. The octree mesh discretizes the domain, and AMR accommodates varying number densities within the domain. CHAOS uses two linear FOTs: Collision-FOT (C-FOT) to satisfy mean free path criteria for DSMC and Electric-FOT (E-FOT) to satisfy Debye length criteria for PIC. Additionally, CHAOS uses multiple CPUs and GPUs for parallel processing, enhancing computational efficiency, particularly for independent tasks like particle mapping.

III. Molecular Dynamics Based Carbon Sputter Model

A. Sputter Yield

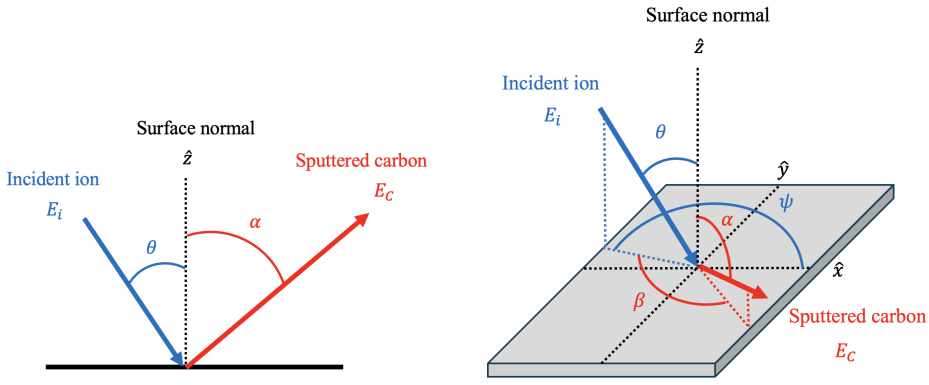

Fig. 1 2D (left) and 3D (right) schematic of sputtering for the MD model[8]

Tran and Chew[5, 6] developed a reduced order carbon sputtering model based on material multi-scale simulation using molecular dynamic (MD) simulations with Monte Carlo (MC) to account for surface morphology effects. Figure 1

shows the coordinate system of the reduced-order carbon sputter model. Assuming that the energy and angular dependence of the sputter yield is independent, we can factor the yields as,

$$Y(E,\theta) = Y(E,0)Y'(\theta). \tag{4}$$

The sputter yield, $Y(E,\theta)$, is computed using the Eckstein and Preuss model [9], and the sputter yield at normal incidence can be expressed as

$$Y(E,0) = Qs_n \frac{\left(\frac{E_i}{E_{th}} - 1\right)^{\mu}}{\left(\frac{\lambda}{w} + \frac{E_i}{E_{th}} - 1\right)^{\mu}}, \tag{5}$$

where Q is a scaling parameter that considers the spread of the impact energy between the ion and target, and λ and μ are the strength and onset of the sputter yield at low ion energy, respectively. The angular dependence can be computed as

$$Y'(\theta) = (\cos(\theta^c))^{-f} \exp\left(b(1 - (\cos(\theta^c)))^{-1}\right), \tag{6}$$

where f is a parameter that scales with the proportion of the particle reflection coefficient and b and c are parameters that control the peak sputter yield angle. The nuclear stopping cross section, s_n, used the Krypton-Carbon (KC) potential form of

$$s_n = \frac{0.5\ln(1 + 1.2288\epsilon)}{\epsilon + 0.1728\sqrt{\epsilon} + 0.0008\epsilon^{0.1504}}, \tag{7}$$

where the reduced nuclear-stopping power, ϵ, is described as

$$\epsilon = \frac{a_L}{Z_i Z_s} \frac{4\pi\epsilon_0}{e^2} \frac{M_s}{M_i + M_s} E_i. \tag{8}$$

The Lindhard screening length, a_L, is given as

$$a_L = \left(\frac{9\pi^2}{128}\right)^{1/3} a_0 \left(Z_i^{2/3} + Z_s^{2/3}\right). \tag{9}$$

Tran and Chew calculated parameters $(Q, \lambda, \mu, E_{th}, b, c, f)$ using MD simulations at different surface morphology and fluence conditions[5]. Our PIC-DSMC study uses their mean value parameters at steady-state sputter yield response because the xenon fluence will be large enough to achieve a steady-state surface morphology during ground testing. In the DSMC simulations, when an ion hits the wall, the sputter yield is calculated using the incident ion information, E_i and θ, with the MD fitted parameters. A sputtering event occurs if a selected random number is lower than the calculated sputter yield.

B. Angular and Energy Distribution of the Sputtered Carbon

If sputtering occurs, the angular and energy distributions of the sputtered carbon determine the sputtered carbon properties. The angular distribution, $f(\alpha)$, in the MD model is based on a linear combination of two Gaussian distributions fitted with the MD simulation results. This gives the polar angle distribution as

$$f(\alpha) = \frac{A}{\sigma_1\sqrt{2\pi}} e^{-\frac{1}{2}\left(\frac{\alpha - \mu_1}{\sigma_1}\right)^2} + \frac{1 - A}{\sigma_2\sqrt{2\pi}} e^{-\frac{1}{2}\left(\frac{\alpha - \mu_2}{\sigma_2}\right)^2}, \tag{10}$$

where $\sigma_1, \sigma_2, \mu_1$, and μ_2 are constants evaluated for the incident ion information, E_i and θ. The Acceptance-Rejection method is used to sample the carbon angular distribution $(f(\alpha))$ as follows.

1) Choose an α value from uniformly distributed from $-\pi/2$ to $\pi/2$.
2) Use the chosen α to get the probability, $f(\alpha)$, with Eq. 10.
3) Choose another random number from uniformly distributed 0 to 1. If this random number is smaller than the probability computed at step 2, accept this α value, see Fig 1. Otherwise, go back to step 1 and repeat the process until the α is accepted.

Similarly, the MD model uses the sputtered energy distribution to determine the sputtered carbon energy. The energy distribution, $g(E_C)$, uses the log-normal (LN) functional form as

$$g(E_c) = \frac{1}{E_c \sigma_s \sqrt{2\pi}} e^{-\frac{1}{2}\left(\frac{\ln(E_c) - \mu_s}{\sigma_s}\right)^2}, \tag{11}$$

where μ_s and σ_s are constants determined by E_i and θ. Tran and Chew performed Maximum Likelihood Estimate (MLE) fitting with MD simulation to determine the constants[5]. The sputtered polar angle (α) is evaluated using the angular PDF, $f(\alpha)$. Then, the energy PDF of the sputtered carbon, $g(E_C)$, is also determined by using the incident ion information, and the computed energy PDF is used to determine the sputtered carbon energy with the Acceptance-Rejection method. The calculated energy will govern the speed of the sputtered carbon. Details of the angular and energy distribution and its sampling to the three-dimensional simulation can be found in a previous study[8].

IV. Simulation Setup

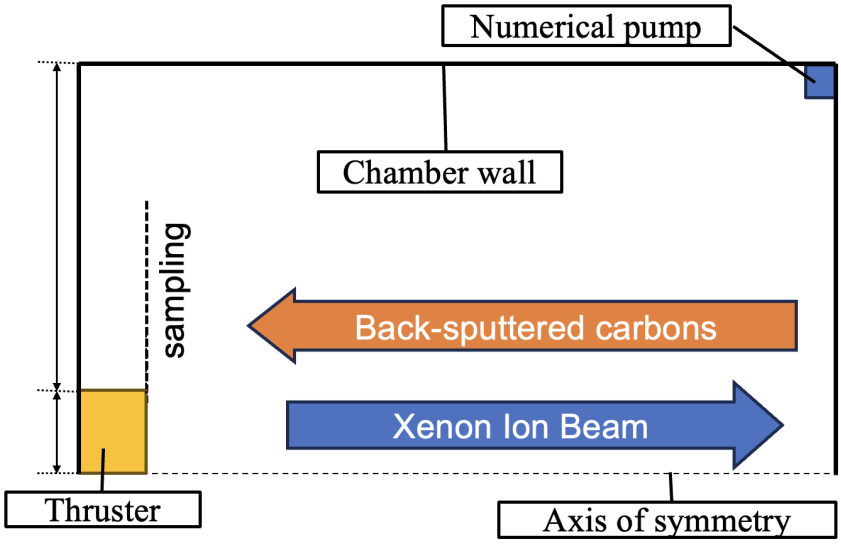

Fig. 2 Simulation setup schematic in $yz-$ plane at $x = 0$.

Table 1 Thruster exit parameters of each species

	Neutrals	Ions
Bulk velocity(m/s)	200	40000
Density (n_{exit}/n_0)	20	1
Temperature (K)	300	-
Inlet type	Half-Maxwellian	Gaussian beam (12°)

In a three-dimensional domain, a xenon ion thruster is located in a cubic vacuum chamber for all simulations. All simulations implement symmetric boundary conditions along the $x-$ and $y-$axis to reduce computation effort. Thus, specular reflection for particles and the Neumann electrical boundary condition for PIC is applied along the $x-$min and $y-$min axis. For collisions with the chamber walls, particles are fully diffusive with 0V Dirichlet electrical boundary conditions. Figure 2 shows the $y-z$ plane of the domain at $x = 0$ and $x-y$ plane of the domain at $z = 0.8$ m.

Table 1 provides the exit conditions of the thruster for each species. The ion number density is $n_0 = 4 \times 10^{13}$ ions/m^3, and neutral number density is 20 times higher than the ion number density. Neutral xenon particles have a velocity

distribution of a full Maxwellian in the $x-$ and $y-$ direction and a half-Maxwellian in the $z-$direction with a bulk velocity of 200 m/s. For the ions, a 12° Gaussian distribution in number density across the radial distance from the thruster center and a bulk velocity of 40,000 m/s in $z-$ direction are applied. The thruster radius of $R_{\text{thruster}} = 0.0625$m is used for all cases.

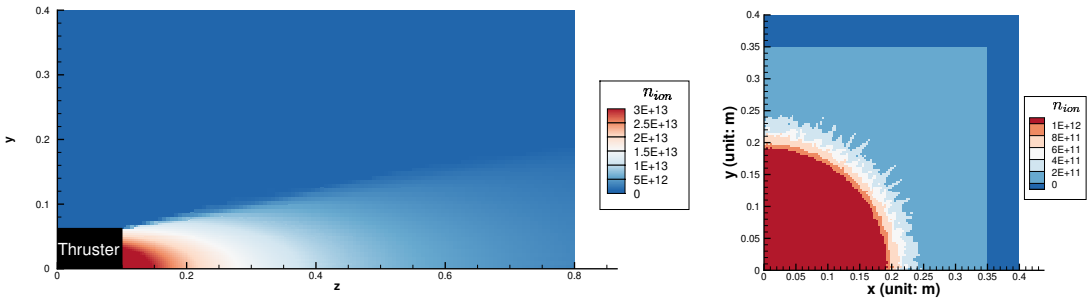

Fig. 3 Xe ion number density contour at $x = 0$ m plane (left) and at beam dump, $z = 0.8$ m (right).

The simulation begins with the PIC-DSMC simulation using both E-FOT and C-FOT. Since the electric field convergence first, the simulation continues without the Poisson solver to save the computational costs. Thus, the simulation only runs DSMC to obtain C-FOT convergence. Figure 3 shows the normalized ion number density contour ain the $x = 0$ plane and at the beam dump. The result shows that most of the ions hit near the center of the beam dump. After the E-FOT and C-FOT reach steady state, the sputtering simulation begins in the PIC-DSMC simulations.

Table 2 Sputter model comparison

	MD model	SE model	MD-ST model	SE-LN model
Threshold energy, E_{th}	10.92 eV[5]	21.0 eV[2]	10.92 eV[5]	21.0 eV[2]
Sputter yield, $Y(E_{\text{i}}, \theta)$	Eckstein with MD fitting[5]	Eckstein with SE fitting[2]	Eckstein with MD fitting[5]	Eckstein with SE fitting[2]
Sputtered angle	MD-fitted angular distribution[5], $f(\alpha)$	angular differential yield[3], $Y'(\theta)$	MD-fitted angular distribution[5], $f(\alpha)$	angular differential yield[3], $Y'(\theta)$
Sputtered energy	MD-fitted energy distribution[6], $g(E_C)$	Sigmund-Thompson[10]	Sigmund-Thompson[10]	MD-fitted energy distribution[6], $g(E_C)$

Table 2 shows the four carbon sputter models used in this study. Nishii and Levin[1] used a semi-empirical fitting Eckstein sputter yield[2] with an angular differential yield[3] and Signmund-Thompson (ST) energy distribution[10, 11] for sputtered carbon energy in the past study, which will be denoted as the SE model. We used the MD and the SE models as two baseline models and performed variations to investigate the effect of energy distribution on back-sputtered carbon flux by implementing variations on these models. MD-ST indicates the change in the energy distribution of the MD model to the ST distribution, and SE-LN indicates the change in the energy distribution of the SE model to the LN function. So, totally four different models: MD, MD-ST, SE, and SE-LN are tested in this study.

In another previous study[8], we compared the SE model with the MD model, and found that the effect of angular distribution is important on the back-sputtered carbon flux, but the effect of energy distribution was not as significant. While the previous study used a sticking coefficient of unity, we further investigated this case with the MD-based sticking coefficients[6] that consider the incident carbon energy and angle to determine the sticking coefficient of carbon to carbon. While we sample all carbons crossing the thruster exit plane, similar to the previous study[8], we further post-processed the result by evaluating the individual carbon atom's energy and incident angle to the thruster exit region. To evaluate whether a carbon atom sticks to the surface, we select the MD sticking coefficient based on the incident carbon atom's energy and angle to the surface. Then we compare that value with a random number selected between [0,1]. If the random number is less than the sticking coefficient, the carbon atom is counted as having stuck to the surface, thereby including it in the carbon deposition rate.

V. Results

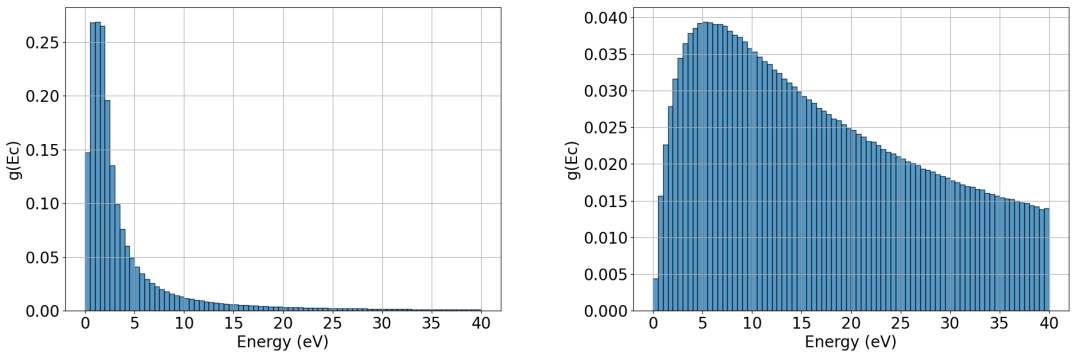

Fig. 4 Back-sputtered carbon energy distribution at thruster exit plane from the simulation with the MD (left) and the SE (right) model.

Figure 4 illustrates the energy distribution of back-sputtered carbon atoms at the thruster exit plane as predicted by the MD and SE models. The MD model employs a LN function fitted with MD data given by Eq. 11, while the SE model is based on the ST distribution[10]. The mean back-sputtered carbon energies are 5.737 eV and 35.259 eV for the MD and SE models, respectively.

As shown in the Figure 4, the MD model demonstrates a high concentration of carbon energies at lower values with a lower standard deviation. In contrast, the SE model predicts a significantly higher mean energy and a broader energy distribution. This discrepancy arises from the inherent differences in the underlying distributions: the ST distribution is not dependent on the incident ion properties and does not adapt to varying conditions, whereas the MD-fitted LN function reflects the dependence on incident ion energy and angle, providing a more realistic representation.

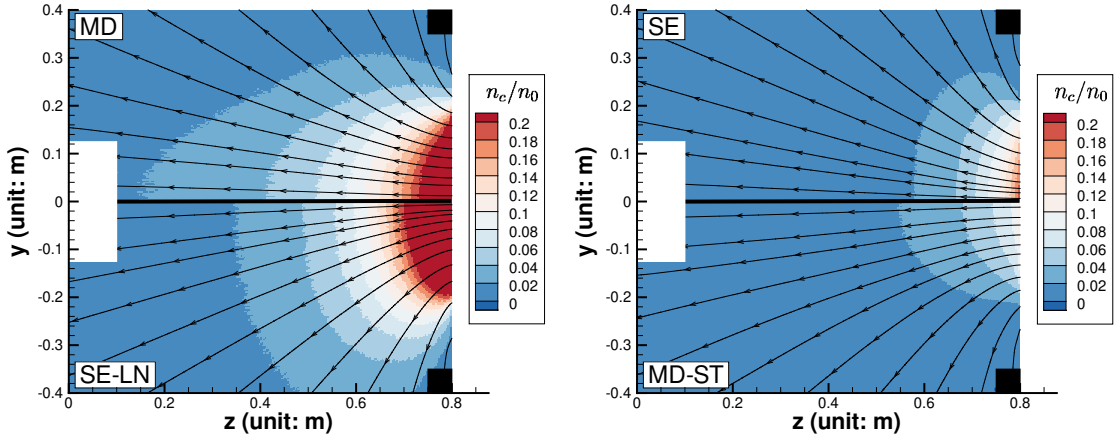

Fig. 5 Carbon number density contours at $x = 0$ of four sputter models: MD(top-left), SE (top-right), SE-LN (bottom-left), and MD-ST (bottom-right) with velocity streamlines. White box at $z = 0$ is where the thruster and plasma screen located and black boxes at $z = 0.8$ are where the numerical pumps located.

Figure 5 presents the carbon number density contours at the $x = 0$ plane for the four sputter models: MD (top-left), SE (top-right), SE-LN (bottom-left), and MD-ST (bottom-right). When we compare the carbon number density contours of models with the same sputtered energy model (ex. MD vs SE-LN or SE vs MD-ST), we can see that the MD model tends to have carbon distribution heading towards to the thruster exit, while the SE model has more a broaden carbon spatial distribution. Thus, the angular distribution method of the sputtered carbons is important in predicting the back-sputtered carbon flux to the thruster.

Furthermore, the models with the MD-based LN function, $g(E_C)$, exhibit higher carbon number densities within the chamber compared to the models with the ST distribution. This difference arises from the sputtered carbon energy distributions. The ST distribution predicts higher carbon energies, resulting in faster-moving carbon particles. In the current CHAOS simulation, a fully sticking boundary condition was applied, meaning carbon particles are removed upon impacting the chamber walls. Consequently, higher-speed particles from the ST distribution are eliminated more quickly, leading to a lower overall carbon number density inside the chamber.

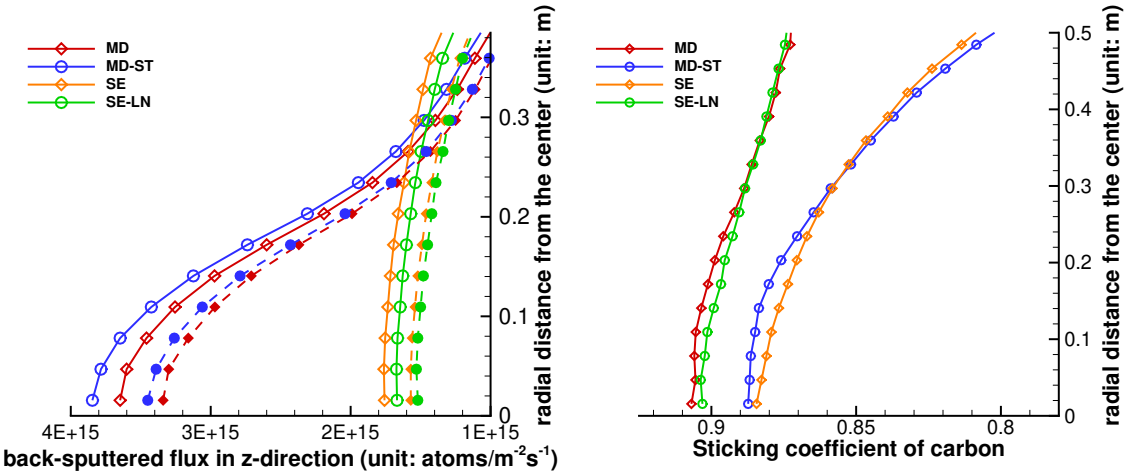

Fig. 6 Back-sputtered carbon flux to the thruster exit plane at $z = 0.1$ m with sticking coefficient of unity as solid lines with empty symbols and with partial sticking coefficient as dashed lines with filled symbols (left), and average sticking coefficient at each probing location (right).

Figure 6 illustrates the back-sputtered carbon flux to the thruster exit plane under different conditions. The left plot represents the carbon flux assuming a sticking coefficient of one obtained from the PIC-DSMC, while the right plot accounts for the MD-derived sticking coefficient by post-processing all sampled carbons. The right plot shows the MD-derived sticking coefficient values sampled during post-processing. As expected, the flux calculated with the MD-based sticking coefficient is lower than that obtained with the full sticking assumption. This reduction occurs because the full sticking assumptions collects all carbon atoms adhere to the surface, resulting in an overestimation of the deposition rate on the thruster exit plane. In contrast, the MD-derived partial sticking assumption captures the realistic behavior of carbon atoms, providing a more accurate assessment of the actual deposition rate.

Additionally, variation in the sticking coefficient at different radial locations is observed. These variations arise because the back-sputtered carbon atoms predominantly originate from beam ions, which are concentrated near the beam dump region of the thruster exit area. At larger radial distances, the average angle of incidence of primary carbon atoms to the thruster exit plane increases. As the incidence angle increases, the sticking coefficient decreases, further reducing the deposition rate.

Table 3 Carbon deposition rate to the thruster ($r < R_{\text{thruster}}$) per beam current (unit: μm/kh $\cdot$ A)

Models	MD	MD-ST	SE	SE-LN
full sticking assumption	59.197	62.313	28.880	27.396
partial sticking assumption (from MD)	53.681	55.300	25.476	24.754

Table 3 provides a summary of the carbon deposition rates at the thruster exit ($z = 0.1$ m) for four models under two different sticking coefficient conditions. These rates are based on the carbon flux within the thruster exit region ($r < R_{\text{thruster}}$). Across all models, the deposition rates decrease by approximately 10 percent when transitioning from full sticking assumption to the MD-derived partial sticking assumptions. Due to the relatively small variation in sticking coefficients in this region, the percentage reduction in deposition rates from the assumption of full sticking to the MD sticking coefficient is consistent across all models.

However, carbon atoms with higher energies, modeled using the ST distribution, tend to exhibit lower sticking coefficients. This discrepancy in sticking coefficients between carbon atoms modeled with the LN function and those modeled with the ST distribution becomes more significant as the angle of incidence increases. This indicates that primary carbon atoms colliding with the sidewalls at high incidence angles are more likely to cause secondary carbon emissions. Although the MD-based sticking coefficient has not been applied as a boundary condition in this study, its future implementation could result in noticeable changes to the deposition rate on the thruster, particularly due to secondary carbon emissions from the sidewalls.

VI. Conclusion

This study examined the effects of different sputter models and energy distributions on back-sputtered carbon flux and deposition rates at the thruster exit in an electric propulsion testing chamber system. The MD-based sputter model showed differences from the SE model, including lower yields, a more centered back-sputtered carbon distribution, and a lower energy profile. The MD model's use of a LN energy distribution resulted in lower mean energies and narrower distributions compared to the ST distribution in the SE model, influencing the transport and deposition patterns of sputtered carbon atoms.

Applying the MD-derived sticking coefficients, which accounts for the incident energy and angle of carbon atoms, reduced the deposition rates at the thruster exit compared to a full sticking coefficient assumption. This effect was more apparent for high-energy and high-incidence angle carbon atoms. Differences in angular and energy distributions between the models also suggest different predictions for secondary carbon emissions from chamber sidewalls.

The findings highlight the importance of angular and energy distributions in predicting back-sputtered carbon flux and deposition rates. Future work will incorporate MD-derived sticking coefficients as boundary conditions in full-scale chamber simulations to better capture the role of secondary emissions. Further research on time-dependent sputtering and chamber wall interactions will refine contamination models for ground testing of electric propulsion systems.

References

[1] Nishii, K., and Levin, D. A., "Three-Dimensional Kinetic Simulations of Carbon Backsputtering in Vacuum Chambers from Ion Thruster Plumes," *Journal of Propulsion and Power*, Vol. 40, No. 1, 2024, pp. 123–137. doi:10.2514/1.B39194, URL https://doi.org/10.2514/1.B39194.

[2] Yim, J. T., "A survey of xenon ion sputter yield data and fits relevant to electric propulsion spacecraft integration," *The 35th International Electric Propulsion Conference*, 2017.

[3] Yim, J. T., "Differential yields and uncertainty assessments for electric propulsion plume impingement sputter redeposition contamination," *The 37th International Electric Propulsion Conference*, 2022.

[4] Jambunathan, R., and Levin, D. A., "CHAOS: An octree-based PIC-DSMC code for modeling of electron kinetic properties in a plasma plume using MPI-CUDA parallelization," *Journal of Computational Physics*, Vol. 373, 2018, pp. 571–604. doi:10.1016/j.jcp.2018.07.005.

[5] Tran, H., and Chew, H. B., "Surface morphology and carbon structure effects on sputtering: Bridging scales between molecular dynamics simulations and experiments," *Carbon*, Vol. 205, 2023, pp. 180–193. doi:https://doi.org/10.1016/j.carbon.2023.01.015, URL https://www.sciencedirect.com/science/article/pii/S0008622323000167.

[6] Tran, H., and Chew, H. B., "Transient to steady-state morphology evolution of carbon surfaces under ion bombardment: Monte Carlo simulations," *Acta Materialia*, Vol. 263, 2024, p. 119498. doi:https://doi.org/10.1016/j.actamat.2023.119498, URL https://www.sciencedirect.com/science/article/pii/S1359645423008273.

[7] Serikov, V., Kawamoto, S., and Nanbu, K., "Particle-in-cell plus direct simulation Monte Carlo (PIC-DSMC) approach for self-consistent plasma-gas simulations," *IEEE Transactions on Plasma Science*, Vol. 27, No. 5, 1999, pp. 1389–1398. doi:10.1109/27.799817.

[8] Lim, G., Tran, H., Levin, D. A., Chew, H. B., and Nishii, K., "Kinetic Simulation of Carbon Sputtering by a Gridded Ion Thruster with a Molecular Dynamics Based Model," *Proceedings of the 38th International Electric Propulsion Conference*, Toulouse, France, 2024.

[9] Eckstein, W., and Preuss, R., "New fit formulae for the sputtering yield," *Journal of Nuclear Materials*, Vol. 320, No. 3, 2003, pp. 209–213. doi:https://doi.org/10.1016/S0022-3115(03)00192-2, URL https://www.sciencedirect.com/science/article/pii/S0022311503001922.

[10] Sigmund, P., "Sputtering by ion bombardment: Theoretical concepts," *Sputtering by Particle Bombardment I: Physical Sputtering of Single-Element Solids*, 1981. doi:10.1007/3540105212_7.

[11] Gnaser, H., *Energy and Angular Distributions of Sputtered Species*, 2007, Vol. 110, pp. 231–328. doi:10.1007/978-3-540-44502-9_5.